Deep Search of the Full O3 LIGO Data for Continuous Gravitational Waves from the Cassiopeia A Central Compact Object

Jonathan Wang[1] and Keith Riles[1]

[1] *University of Michigan Physics Department, Ann Arbor, MI 48109, USA*

(compiled September 29, 2024)

We present the deepest search to date for continuous gravitational waves from the neutron star in the Cassiopeia A (Cas A) supernova remnant, using the full LIGO data set from the LIGO-Virgo-KAGRA (LVK) third observing run (O3). We use the Weave semi-coherent method with a first-stage coherence time of 30 days while restricting the search band to 20–200 Hz for assumed source ages greater than 300 years, substantially improving upon the sensitivity of a previous Weave-based search for this source. No gravitational wave signal is detected. Estimates from simulated continuous wave signals indicate we achieve the most sensitive results to date across the explored parameter space volume, probing to a median strain magnitude as low as 4×10^{-26} for frequencies near 200 Hz at 95% confidence level. The method presented here provides a template for future searches for Cas A and other central compact objects of interest using data from the ongoing fourth LVK run (O4). LIGO-P2400236-v2

I. INTRODUCTION

A prior search [1] in LIGO data from the third LIGO-Virgo-KAGRA (LVK) observing run (O3) for continuous gravitational waves from the neutron stars at the centers of the Cassiopeia (Cas A, G111.7−2.1) [2] and Vela Jr. (G266.2−1.2) [3] supernova remnants yielded the deepest strain sensitivity to date for both sources. That search used the Weave [4] semi-coherent program with 5-day and 7.5-day coherence times, respectively, to probe the first six months of O3 data for signal frequencies between 20 and 976 Hz.

Here we report the results of a significantly deeper demonstration search for a Cas A signal in the 20-200 Hz band, one that uses a 30-day coherence time to improve sensitivity. The new search also uses the full 11 months of data from the LIGO [5], Virgo [6] and KAGRA [7] third observation run (O3). This demonstration of sensitivity improvement paves the way for still-deeper searches of the lower-noise data from the ongoing fourth LVK observing run (O4). In addition, the successful deployment of the program on the Open Science Grid (OSG) [8–11] for this analysis offers a path to greater computational resources for future searches of the O4 data.

While the longer observing and coherence times used in this search provide substantial gain in sensitivity, that gain comes at a significant computation cost. As a result, in this demonstration analysis, we restrict the search band to lower frequencies, typical of known young pulsars [12]. As a result, over the band searched, we obtain substantially improved sensitivity for Cas A with respect to all previous searches of O1, O2 and O3a LIGO and Virgo data [1, 13–19]. Recent reviews of continuous wave (CW) search methodology include [20–24].

Cas A, at just over 300 years old [25, 26]. is an extremely young object, making it the target of multiple searches for continuous gravitational waves since 2010 [1, 13–19], because it may retain a high rotation frequency and may possess an appreciable non-axisymmetry from its recent birth [27–34]. Continuous emission due to unstable r-modes is also possible in such a young star [35–39].

Because of the enormous pressure on its nuclear matter, one expects a neutron star to assume a highly spherical shape in the limit of no rotation and, with rotation, to form an axisymmetric oblate spheroid. A number of physical processes can disrupt the symmetry, however, to produce quadrupolar gravitational waves from the stellar rotation. Those processes include crustal distortions from cooling or accretion, buried magnetic field energy and excitation of r-modes. Comprehensive reviews of continuous gravitational wave emission mechanisms from neutron stars can be found in [40, 41].

Central compact objects (CCOs) at the cores of supernova remnants present interesting potential sources, especially those in remnants inferred from their sizes and expansion rates to be young. The Cas A remnant contains such an object, thought to be a young neutron star. One can derive an estimated age-based upper limit[1] on a CCO's continuous-wave strain amplitude by assuming the star's current rotation frequency is much lower than its rotation frequency at birth and that the star's spin-down since birth has been dominated by gravitational wave energy loss ("gravitar" emission) [42]:

$$h_{\rm age} = (2.3 \times 10^{-24}) \left(\frac{1\,\mathrm{kpc}}{r}\right) \sqrt{\left(\frac{1000\,\mathrm{yr}}{\tau}\right)\left(\frac{I_{zz}}{I_0}\right)}, \quad (1)$$

where r is the distance to the source, τ is its age and I_{zz} is the star's moment of inertia about its spin axis, with a fiducial value of $I_0 = 10^{38}$ kg· m^2.

Cas A is perhaps the most promising example of a potential gravitational wave CCO source in a supernova

[1] This strain estimate gives a rough benchmark upper limit on what is possible in an optimistic scenario; its assumption that current rotation frequency is small relative to the star's birth frequency is less plausible for higher frequencies.

remnant. Its birth aftermath may have been observed by Flamsteed [25] ∼340 years ago in 1680, and the expansion of the visible shell is consistent with that date [26]. Hence Cas A, which is visible in X-rays [43, 44] but shows no pulsations [45], is almost certainly a very young neutron star at a distance of about 3.3 kpc [46, 47]. From equation 1, one finds an age-based strain limit of $\sim 1.2\times10^{-24}$, which is readily accessible to LIGO and Virgo detectors in their most sensitive band.

The remainder of this article is organized as follows: Section II describes the data set used. Section III briefly describes the Weave search program [4] which uses semi-coherent summing of a matched-filter detection statistic known as the $\mathcal{F}$-statistic [48]. Section IV presents the results of the search, which are upper limits on the gravitational wave strain amplitude *vs.* frequency, along with derived, model-dependent upper limits on stellar ellipticity and r-modes amplitude. Section V concludes with a discussion of the results and prospects for future searches.

II. DATA SETS USED

Advanced LIGO consists of two detectors, one in Hanford, Washington (designated H1), and the other in Livingston, Louisiana (designated L1), separated by a ∼3000-km baseline [5]. Each site hosts one, 4-km-long interferometer inside a vacuum envelope with the primary interferometer optics suspended by a cascaded, quadruple suspension system, affixed beneath an in-series pair of suspended optical tables, in order to isolate them from external disturbances. The interferometer mirrors act as test masses, and the passage of a gravitational wave induces a differential-arm length change which is proportional to the gravitational-wave strain amplitude.

The third Advanced LIGO and Virgo data run (O3) began April 1, 2019 and ended March 27, 2020. The first six months (April 1, 2019 to October 1, 2019), prior to a 1-month commissioning break, is designated as the O3a period, and the final, approximately five-month period starting November 1, 2019 is designated as O3b. Here we use both the O3a and O3b data sets for a full-O3 analysis. The Virgo data has not been used in this analysis because of an unfavorable tradeoff in computational cost for sensitivity gain, given the interferometer's higher noise level during the O3 run. The systematic error in the amplitude calibration is estimated to be lower than 7% (68% confidence interval) for both LIGO detectors over all frequencies throughout O3a [49].

Prior to searching the O3 data for CW signals, the quality of the data was assessed and steps taken to mitigate the effects of instrumental artifacts. As in previous Advanced LIGO observing runs [50], instrumental "lines" (sharp peaks in fine-resolution, run-averaged H1 and L1 spectra) are marked, and where possible, their instrumental or environmental sources identified [51]. The resulting database of artifacts proved helpful in eliminating spurious signal candidates emerging from the search; no bands were vetoed *a priori*, however.

As discussed in [1, 52], another type of artifact observed in the O3 data for both H1 and L1 were relatively frequent and loud "glitches" (short, high-amplitude instrumental transients) with most of their spectral power lying below ∼500 Hz. To mitigate the effects of these glitches on O3 CW searches for signals below 475 Hz, a simple glitch-gating algorithm was applied [53, 54] to excise the transients from the data.

III. ANALYSIS METHOD

This search relies upon semi-coherent averaging of $\mathcal{F}$-statistic [48] values computed for 11 30-day segments spanning the O3 run period (excluding the October 20219 commissioning break. Section III A describes the signal model used in the analysis. Section III B describes the mean $\mathcal{F}$-statistic detection statistic at the core of the analysis. Section III C describes the Weave infrastructure for summing individual $\mathcal{F}$-statistic values over the observation period, including the configuration choices for the searches presented in this article. Section III D describes the procedure used to follow up on outliers found in the first stage of the hierarchical search. The methodology is very similar to that used in the previous LVK O3a search for Cas A, but the much longer coherence time used here in the initial stage (30 days *vs.* the prior 5 days) warrants the incorporation of a third frequency derivative into the search parameter space at the first stage of follow-up.

A. Signal model and parameter space searched

The signal templates assume a classical model of a spinning neutron star with a time-varying quadrupole moment that produces circularly polarized gravitational radiation along the rotation axis, linearly polarized radiation in the directions perpendicular to the rotation axis and elliptical polarization for the general case. The strain signal model $h(t)$ for the source, as seen by the detector, is assumed to be the following function of time t:

$$\begin{aligned} h(t) \;=\; h_0\big(F_+(t,\alpha_0,\delta_0,\psi)\frac{1+\cos^2(\iota)}{2}\cos(\Phi(t)) \\ +F_\times(t,\alpha_0,\delta_0,\psi)\cos(\iota)\sin(\Phi(t))\big)\;, \end{aligned} \tag{2}$$

In Eq. 2, h_0 is the intrinsic strain amplitude, $\Phi(t)$ is the signal phase, F_+ and $F_\times$ characterize the detector responses to signals with "+" and "×" quadrupolar polarizations [55], and the sky location is described by right ascension α_0 and declination δ_0. In this equation, the star's orientation, which determines the polarization, is parametrized by the inclination angle ι of its spin axis relative to the detector line-of-sight and by the angle ψ of the axis projection on the plane of the sky. The linear polarization case ($\iota = \pi/2$) is the most unfavorable because the gravitational wave flux impinging on the detectors is smallest for an intrinsic strain amplitude h_0,

possessing eight times less incident strain power than for circularly polarized waves ($\iota = 0,\ \pi$).

In a rotating triaxial ellipsoid model for a star at distance r spinning at frequency $f_{\rm rot}$ about its (approximate) symmetry axis (z), the amplitude h_0 can be expressed as

$$h_0 = \frac{4\,\pi^2 G \epsilon I_{\rm zz} f^2}{c^4 r} \quad (3)$$

$$= [1.1\times10^{-24}]\Big[\frac{\epsilon}{10^{-6}}\Big]\Big[\frac{I_{\rm zz}}{I_0}\Big]\Big[\frac{f}{1\,{\rm kHz}}\Big]^2\Big[\frac{1\,{\rm kpc}}{r}\Big], \quad (4)$$

for which the gravitational radiation is emitted at frequency $f = 2\,f_{\rm rot}$. The equatorial ellipticity ϵ is a useful, dimensionless measure of stellar non-axisymmetry:

$$\epsilon \equiv \frac{|I_{xx} - I_{yy}|}{I_{zz}}. \quad (5)$$

Unstable r-mode emission [35–39] at gravitational wave frequency f (which for this model is $\sim(4/3)f_{\rm rot}$) can be parametrized by a dimensionless amplitude α governing the strain amplitude [56]:

$$h_0 = [3.6\times10^{-23}]\Big[\frac{\alpha}{0.001}\Big]\Big[\frac{f}{1\,{\rm kHz}}\Big]^3\Big[\frac{1\,{\rm kpc}}{r}\Big]. \quad (6)$$

The phase evolution of the signal is given in the reference frame of the Solar System barycenter (SSB) by the fourth-order approximation:

$$\Phi(t) = 2\pi\big[f\cdot(t-t_0) + \frac{1}{2}\dot{f}\cdot(t-t_0)^2 + \frac{1}{6}\ddot{f}\cdot(t-t_0)^3 + \frac{1}{24}\dddot{f}\cdot(t-t_0)^4\big] + \phi_0\ , \quad (7)$$

where f is the SSB source frequency, $\dot{f}$ is the first frequency derivative (which, when negative, is termed the spin-down), $\ddot{f}$ and $\dddot{f}$ are the second and third frequency derivatives, t is the SSB time, and the initial phase ϕ_0 is computed relative to reference time t_0 (taken here to be the approximate mid-point of the O3 period: 2019 September 28 15:07:45 UTC – GPS 1253718483). When expressed as a function of the local time of ground-based detectors, Eq. 7 acquires sky-position-dependent Doppler shift terms [48].

In this analysis, we search a band of gravitational wave signal f from 20 to 200 Hz and a frequency derivative $\dot{f}$ range governed by the assumed minimum age τ of the source. Detector noise deteriorates badly below 20 Hz because of ground motion. The long coherence time used in the initial stage of this search makes it computationally much more costly at each frequency range than the previous LVK search [1]. To reduce total computational cost, we search only up to 200 Hz, a range that covers the most promising band for a young, non-recycled neutron star [23]. Similar previous searches [13–15] have assumed a power law spin-down: $\dot{f} \propto -f^n$ with braking index n, with n taking on values of 3 for magnetic dipole emission, 5 for GW quadrupole emission (gravitar) and 7 for r-mode emission. For a source that begins at a high frequency and spins down to a much lower present-day frequency with a constant braking index, one expects $\dot{f} \approx \frac{1}{n-1}(f/\tau)$. Allowing for n to range between 2 and 7 because of multiple potential spin-down contributions leads to the search range:

$$-\frac{f}{\tau} \le \dot{f} \le -\frac{1}{6}\frac{f}{\tau}, \quad (8)$$

which has been assumed in several previous searches [13–15]. Here, as was done in the O3a LVK search [1], we take a slightly more conservative approach, allowing the upper limit on $\dot{f}$ to reach zero, at modest additional computational cost, while allowing for some time-dependent braking indices and uncertainties in the source's effective age. The range in second frequency derivative $\ddot{f}$ is determined for any frequency f and first derivative $\dot{f}$ by the same relation used in previous searches (governed by the braking index range considered):

$$2\frac{\dot{f}^2}{f} \le \ddot{f} \le 7\frac{\dot{f}^2}{f}. \quad (9)$$

In outlier follow-up stages in which a non-negligible third derivative $\dddot{f}$ is probed, the range is governed by the braking index consistent with the outlier's nominal f, $\dot{f}$ and $\ddot{f}$ values.

Table I lists the maximum absolute values of $\dot{f}$ and $\ddot{f}$ at the lowest and highest search frequencies, along with the right ascensions and declinations used in the Cas A search.

Source	Cassiopeia A [57]
Right ascension	23h 23m 27.85s
Declination	+58° 48' 42.8"
Max. $\dot{f}$ (Hz/s) @20 Hz	2.2×10^{-9}
Max. $\dot{f}$ (Hz/s) @200 Hz	2.1×10^{-8}
Max. $\ddot{f}$ (Hz/s^2) @20 Hz	1.7×10^{-18}
Max. $\ddot{f}$ (Hz/s^2) @200 Hz	1.6×10^{-17}

TABLE I. Sky locations and maximum $\dot{f}$, $\ddot{f}$ values used in the Cas A search at the lowest and highest frequencies.

B. The mean $\mathcal{F}$-statistic

This search is based on a semi-coherent average of $\mathcal{F}$-statistic values over many individual intervals of the approximately 11-month observing period spanning nearly 12 calendar months. Within each segment of coherence time duration $T_{\rm coh}$, the $\mathcal{F}$-statistic [48] is computed as in previous searches, as a detection statistic proportional

to the signal amplitude h_0^2, maximized over linear amplitudes that are functions of h_0, the unknown orientation angles ι and ψ, and the phase constant ϕ_0. In Gaussian noise with no signal present, the value of $2\mathcal{F}$ follows a χ^2 distribution with four degrees of freedom and has an expectation value of four. The presence of a signal leads to a non-central χ^2 distribution with a non-centrality parameter proportional to $h_0^2 \cdot T_{\rm coh}$ and inversely proportional to the average power spectral density of the detector noise. The non-centrality parameter, which is the expectation value of the *excess* $\mathcal{F}$-statistic $(2\mathcal{F} - 4)$, also depends on the source's orientation and sky location, and on the orientations and locations of the LIGO interferometers [48].

We compute a semi-coherent mean $\mathcal{F}$-statistic we call $2\bar{\mathcal{F}}$ from the average value of $2\mathcal{F}$ over the $N_{\rm seg}$ (=11) segments into which the observing period is divided:

$$2\bar{\mathcal{F}} = \frac{1}{N_{\rm seg}} \sum_{i=1}^{N_{\rm seg}} 2\mathcal{F}. \tag{10}$$

In the absence of signal, this detection statistic too has an expectation value of four, but has the underlying shape of a χ^2 distribution with $4N_{\rm seg}$ degrees of freedom with a (rescaled) standard deviation of $\sqrt{8/N_{\rm seg}}$. The presence of a signal leads to an offset in the mean that is approximately the same as the non-centrality parameter above, for a fixed $T_{\rm coh}$.

C. The Weave infrastructure

The Weave software infrastructure provides a systematic approach to covering the parameter space volume in a templated search to ensure acceptable loss of signal-to-noise ratio (SNR) for true signals lying between template points [4]. The Weave program combines together recent developments in template placement to use an optimal parameter-space metric [58, 59] and optimal template lattices [60]. The package is versatile enough to be used in all-sky searches for unknown sources. Here we use a simpler configuration applicable to well localized sources, such as Cas A.

In brief, a template grid in the parameter space is created for each time segment, a grid that is appropriate to computing the $\mathcal{F}$-statistic for a coherence time $T_{\rm coh}$ equal to the total observation period $T_{\rm obs}$ divided by $N_{\rm seg}$. The spacing of the initial grid points in $(f,\ \dot{f},\ \ddot{f})$ is set according to a metric [58, 59] that ensures a worst-case maximum mismatch $m_{\rm coh}$ defined by the fractional loss in $2\mathcal{F}$ value due to a true signal not coinciding with a search template.

Separately, a much finer grid is defined for the full observation period with respect to the midpoint of the observation period, one with its own mismatch parameter $m_{\rm semi-coh}$, analogous to $m_{\rm coh}$, but defined to be the average of the coherent mismatch values over all segments [59]. It choice is set empirically in a tradeoff between sensitivity and computational cost. The Weave package creates at initialization a mapping between each point in the semi-coherent template grid and a nearest corresponding point in each of the separate, coarser segment grids, accounting for frequency evolution. The semi-coherent detection statistic $2\bar{\mathcal{F}}$ is constructed for each semi-coherent template from this mapping [4].

For the Cas A search presented here, a simulation study was carried out to evaluate tradeoffs in achievable sensitivity for a variety of segment lengths ($T_{\rm coh}$) and mismatch parameters $m_{\rm coh}$ and $m_{\rm semi-coh}$, with a goal of staying within a maximum total computational cost of ∼3 million CPU core hours. In the end, we chose the Weave configuration parameters shown in Table II, with 60-day and 120-day follow-ups. Because of the commissioning break following O3a, one 60-day segment and one 120-day segment spanned part or all of the month of absent data, leading to a significantly lower livetime for that segment and hence a lower expected excess $\mathcal{F}$-statistic contribution due to a true signal.

Search jobs are carried out in 0.1-Hz bands of f, with further divisions into $(\dot{f},\ddot{f})$ sub-ranges, as needed, to ensure the total memory required for a job not exceed 16 GB. In practice, this constraint was met by determining the total number of coherent-stage templates needed to cover each 0.1-Hz band and then dividing the $\dot{f}$ and $\ddot{f}$ ranges to achieve approximately 2×10^9 templates per job.

D. Outlier follow-up

Each individual job returns the $(f,\dot{f},\ddot{f})$ values of the 1000 templates ("top-list") with the largest ("loudest") $2\bar{\mathcal{F}}$ values. For 0.1-Hz bands with $N_{\dot{f}\ddot{f}}$ divisions by $\dot{f}$ and $\ddot{f}$, there are $N_{\dot{f}\ddot{f}} \times 1000$ values returned. Outlier templates to be followed up are those in these top-lists exceeding a frequency-dependent threshold $2\bar{\mathcal{F}}_{\rm thresh}(f)$ which rises slowly with f as the number of distinct templates searched grows, thereby increasing the statistical trials factor. A nominal threshold is set based on the signal-free χ^2 distribution with four degrees of freedom per segment such that the expectation value of outliers is one per 1-Hz band in Gaussian noise, given the empirically obtained trials factor based on the total number of semi-coherent templates to search. We use an $\mathcal{F}$-statistic threshold that rises monotonically from about 14.47 at 20 Hz to about 15.44 at 200 Hz.

In practice, non-Gaussian artifacts lead to much higher outlier counts in particular bands contaminated by instrumental line sources (Sect. II). In some cases strong instrumental lines can lead to more than 1000 templates from a single job that exceed the threshold for a particular 0.1-Hz band and range of $(\dot{f},\ddot{f})$ searched. We refer to those cases as "saturated" since potentially interesting templates may be suppressed by the top-list cap. Each of those cases is examined manually to assess instrumental contamination. Where such contamination is confirmed, those 0.1-Hz bands are marked and excluded from those

Parameter	Cas A
Coherent mismatch $m_{\rm coh}$	0.1
Semi-coherent mismatch $m_{\rm semi-coh}$	0.2
Coherence time (number of segments) for initial search	30 days (11)
Coherence time (number of segments) for 1st follow-up	60 days (6)
Coherence time (number of segments) for 2nd follow-up	120 days (3)

TABLE II. WEAVE configuration parameters used for the Cas A search.

for which we quote upper limits below. The appendix lists these 0.1-Hz bands.

For non-saturated sub-ranges of individual 0.1-Hz bands, outliers exceeding the threshold $2\bar{\mathcal{F}}_{\rm thresh}(f)$ are collected together in 1-Hz bands for clustering in the $(f,\dot{f})$ plane before proceeding to outlier follow-up. The clustering is carried out using an iterative *K-means* algorithm [61] with a maximum allowed cluster count of 1000. The particular K-means implementation uses the scikit python library [62], where the $\dot{f}$ values are rescaled by a factor of about -1.3×10^{-7} to give comparable ranges in f and $\dot{f}$ numerical values to assist 2-dimensional clustering. A maximum of 1000 clusters are permitted per 1-Hz band.

The loudest outlier in each cluster is then followed up by doubling the coherence time from 30 days (11 segments) to 60 days (6 segments) and searching in a narrowed region of parameter space in f, $\dot{f}$ and $\ddot{f}$ around the outlier's nominal values, but also allowing for a non-zero $\dddot{f}$, given the increased importance of the 3rd derivative for the longer coherence time. An outlier is deemed to pass this first stage of follow-up if its loudest outlier has an excess mean $\mathcal{F}$-statistic 70% or more greater than its initial value. For a true signal, the expectation value of the excess mean $\mathcal{F}$-statistic is proportional to the coherence time and hence doubles with a doubled coherence time. Lowering the threshold on the ratio of the increase from 2.0 to 1.7 allows both for the intrinsic spread of the mean $\mathcal{F}$-statistic distribution and for the fact that one of the 60-day segments overlaps substantially with the mid-run commissioning break. Pursuing only the loudest survivor per initial outlier preserves high detection efficiency for a true signal while reducing computational cost from following up multiple candidate templates contaminated by the same instrumental disturbance.

Each loudest surviving outlier is then passed to a second stage of follow-up in which the coherence is again doubled, to 120 days (3 segments), and again the excess mean $\mathcal{F}$-statistic is required to increase by 70% or more. Survivors of the 2nd follow-up stage are inspected manually for spectral artifacts. More quantitatively, the ratio of excess $\mathcal{F}$-statistic in H1 data with respect to L1 data is assessed for consistency with an astrophysical source. The distribution of this ratio is subject to noise fluctuations and varies with frequency, expecially below 50 Hz where H1's noise level is more elevated than L1's. Since the expected excess $\mathcal{F}$-statistic for a true signal scales as the inverse of the power spectral density, we define a noise-normalized ratio:

$$R^{\rm H/L}_{\rm norm} = \frac{(\mathcal{F}-4)_{\rm H1}S_h^{\rm H1}}{(\mathcal{F}-4)_{\rm L1}S_h^{\rm L1}}, \tag{11}$$

where the power spectral densities $S_h^{\rm H1,L1}$ are weighted averages (see section IV below) over 1 Hz bands containing the outliers. The distribution of the ratio peaks for a true astrophysical signal at ∼1.68 and has a standard deviation of ∼0.25 for signal simulations with strengths comparable to those corresponding to 95% upper limits (see section IV). The larger expected excess mean $\mathcal{F}$-statistic for H1 is due to its more favorable time-averaged antenna pattern function for a source at the Cas A sky location. Based on these injections, we require an outlier to have its $R^{\rm H/L}_{\rm norm}$ value lie between 1.05 and 2.35 (see Figure 1).

IV. SEARCH RESULTS

The search described above was carried out on the full O3 data for the Cas A source. Excluding saturated sub-bands, there were ∼56,000 outliers above threshold following clustering. These outliers were all followed up with a narrowed search and a doubling of the coherence time. An outlier was considered to survive follow-up if the loudest candidate template from its follow-up displayed an increase of 70% or more in excess $2\bar{\mathcal{F}}$ with respect to the original outlier's excess $2\bar{\mathcal{F}}$. This criterion led to 1228 first-stage follow-up survivors. A second stage of follow-up requiring another 70% increase in excess mean $\mathcal{F}$-statistic led to only 34 survivors, grouped into 15 clusters. The putative source parameters for the loudest outlier in each surviving cluster are listed in Table III.

Figure 2 shows the Cas A outlier and survivor counts in 1-Hz bands for the multiple stages of analysis, starting with outliers exceeding the threshold $2\bar{\mathcal{F}}_{\rm thresh}(f)$ and proceeding to those surviving the successive requirements that the excess $2\bar{\mathcal{F}}$ increase by 70% each stage of follow-up. Saturated sub-bands listed in the appendix are shaded.

Strain histograms [1] were inspected for each of the final 34 survivors to assess qualitatively any obvious con-

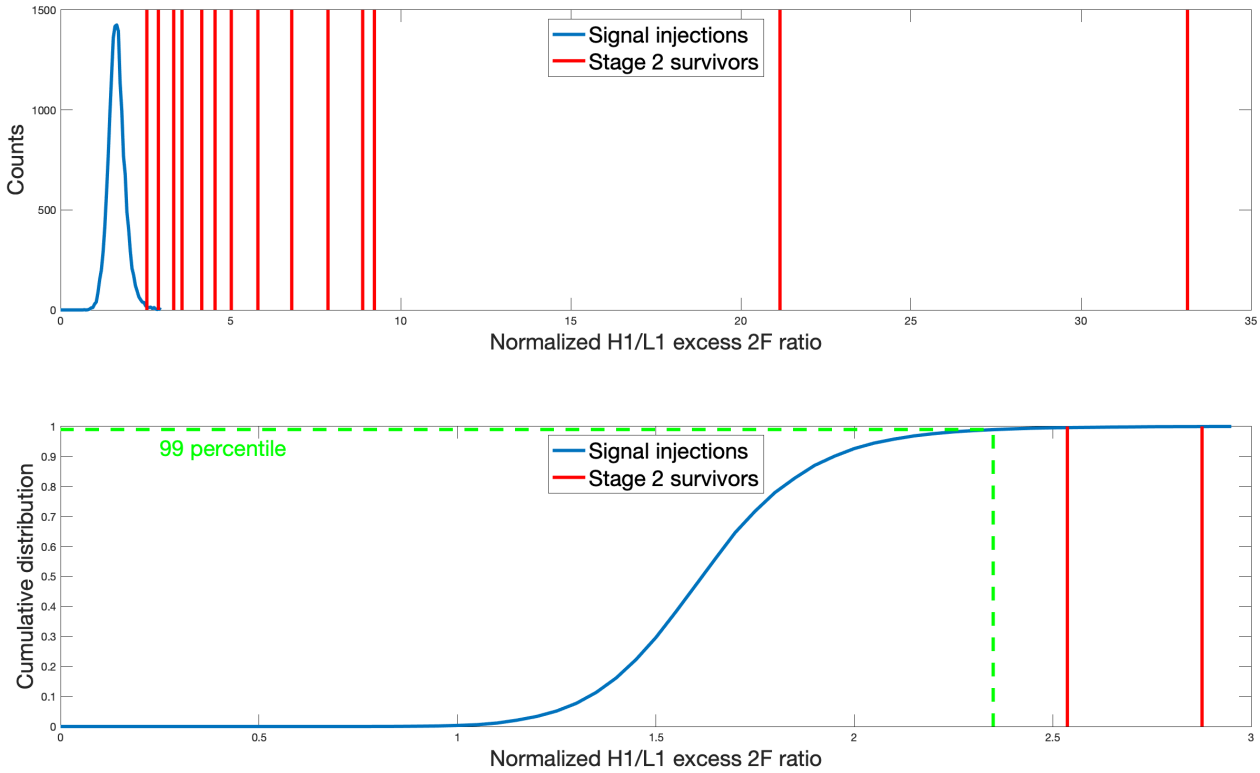

FIG. 1. *Upper panel:* Distribution of the ratio $R^{\mathrm{H/L}}_{\mathrm{norm}}$ of excess mean $\mathcal{F}$-statistic for H1 data alone divided by that for L1 data alone and normalized by average power spectral densities after the 2nd stage of follow-up (three 120-day segments). The blue solid curve shows the distribution for 1.6×10^4 injections, and the red vertical bars show the corresponding ratios for the 15 survivors of the 2nd stage of follow-up. The H1 excess mean $\mathcal{F}$-statistic should be larger than that of L1 because H1 has a more favorable time-averaged antenna pattern. *Lower panel:* Cumulative distribution of the ratio for injections (blue solid curve) along with individual values for stage-2 survivors with ratios below 3. The dashed green lines indicate the 99 percentile of ratios found for the injections. None of the 15 survivors is consistent with the signal injection distribution. (color online).

tributing detector artifacts. An example histogram is shown in Fig. 3 in which spectral line artifacts in the H1 interferometer are apparent. Similar artifacts are visible for 9 of the 15 surviving clusters. Table IV indicates which outliers display such artifacts.

A more quantitative assessment comes, however, from examining the ratio of the H1 excess mean $\mathcal{F}$-statistic to the L1 excess mean $\mathcal{F}$-statistic, also shown in Table IV. Imposing the requirement (section III D that the ratio lie between 1.05 and 2.35 eliminates all 15 outliers. The distribution of the ratio for the outliers is shown in Fig. 1, along with the distribution expected from astrophysical signals.

We conclude that there is no significant evidence in this analysis for a continuous wave signal from the compact object at the center of the Cas A supernova remnant.

Given the absence of a detection, we derive optimistic strain upper limits in each 1-Hz band at 95% confidence level on the assumption that no signal was detected with a mean $\mathcal{F}$-statistic above the initial nominal threshold (14.47-15.44, see section III D) and more conservative upper limits based on the loudest initial outlier even though all outliers above the nominal threshold were followed up after clustering and eliminated. The conservative upper limits are presented to allow for the possibility that an astrophysical signal exceeding the nominal threshold was eliminated in the initial outlier clustering procedure because of nearness to a loud instrumental artifact.

In each case, upper limits are derived from a set of 1000 injections of varying strain magnitudes in a range bracketing the expected 95% strain sensitivity value are used to determine an estimated upper limit with a statistical uncertainty of typically 4%. Figure 4 shows the resulting upper limits where an uncertainty band is also shown using the quadrature of each optimistic upper limit's statistical error and the 7% systematic calibration uncertainty [49]. Also shown are prior sensitivity results from the Weave-based O3a search [1] and upper limits or sensitivities for other searches [16, 18, 19] of Advanced LIGO data sets.

Outlier	f (Hz)	$\dot{f}$(Hz/s)	$\ddot{f}$(Hz/s^2)	$\dddot{f}$(Hz/s^3)
1	53.7159	-3.060×10^{-9}	6.556×10^{-19}	-2.436×10^{-28}
2	56.7051	-5.377×10^{-9}	1.537×10^{-18}	-7.324×10^{-28}
3	56.5997	-4.908×10^{-9}	2.127×10^{-18}	-1.659×10^{-27}
4	56.9888	-1.413×10^{-9}	1.838×10^{-19}	-4.324×10^{-29}
5	60.7184	-5.800×10^{-11}	9.073×10^{-21}	-2.830×10^{-30}
6	68.6976	-1.353×10^{-9}	1.946×10^{-19}	-5.213×10^{-29}
7	72.0103	-5.515×10^{-10}	2.335×10^{-20}	-1.799×10^{-30}
8	74.6357	-4.265×10^{-10}	5.921×10^{-20}	-1.610×10^{-29}
9	85.7683	-3.598×10^{-9}	9.536×10^{-19}	-4.655×10^{-28}
10	89.9197	-5.359×10^{-10}	1.248×10^{-20}	-5.067×10^{-31}
11	96.0999	-6.823×10^{-9}	2.929×10^{-18}	-2.306×10^{-27}
12	99.6590	-6.386×10^{-10}	1.536×10^{-20}	-6.407×10^{-31}
13	128.5795	-1.164×10^{-10}	2.025×10^{-20}	-7.031×10^{-30}
14	128.0435	-2.720×10^{-9}	4.028×10^{-19}	-1.107×10^{-28}
15	150.2169	-1.145×10^{-8}	2.600×10^{-18}	-9.829×10^{-28}

TABLE III. Frequency parameters for the surviving Cas A outliers from stage 2 follow-up.

Outlier	$\mathcal{F}^{\mathrm{HL}}_{\mathrm{excess}}$ (30 days)	$\mathcal{F}^{\mathrm{HL}}_{\mathrm{excess}}$ (60 days)	$\mathcal{F}^{\mathrm{HL}}_{\mathrm{excess}}$ (120 days)	$\mathcal{F}^{\mathrm{H}}_{\mathrm{excess}}$ (120 days)	$\mathcal{F}^{\mathrm{L}}_{\mathrm{excess}}$ (120 days)	$R^{\mathrm{H/L}}_{\mathrm{norm}}$ (120 days)
1	11.24	20.00 (1.78)	34.12 (1.71)	23.30	11.18	3.33
2	11.52	21.16 (1.84)	40.30 (1.91)	36.65	9.19	5.80
3	11.26	19.46 (1.73)	33.72 (1.73)	26.34	10.73	3.57
4	11.30	19.40 (1.72)	35.25 (1.82)	26.62	13.46	2.88
5	11.04	19.29 (1.75)	33.54 (1.74)	42.08	1.91	385.73
6	11.64	20.44 (1.76)	35.01 (1.71)	38.11	6.61	8.88
7	11.06	19.20 (1.74)	32.69 (1.70)	38.11	1.72	33.13
8	11.86	20.89 (1.76)	35.65 (1.71)	35.12	7.61	6.80
9	11.40	19.64 (1.72)	34.75 (1.77)	20.96	12.09	2.54
10	11.20	19.26 (1.72)	32.79 (1.70)	40.20	4.02	21.15
11	11.18	19.24 (1.72)	34.45 (1.79)	25.17	9.02	4.15
12	11.45	19.80 (1.73)	34.20 (1.73)	33.24	5.76	9.23
13	11.58	21.18 (1.83)	37.47 (1.77)	38.22	10.85	4.54
14	11.52	19.81 (1.72)	34.83 (1.76)	32.10	5.27	7.86
15	12.44	21.18 (1.70)	36.10 (1.70)	30.72	7.92	5.02

TABLE IV. Combined H1-L1 excess mean $\mathcal{F}$-statistic values search stage and two follow-up stages, along with individual H1 and L1 excess mean $\mathcal{F}$-statistic values and their ratios for the 2nd follow-up stage, shown for the surviving Cas A outliers from stage 2 follow-up (see Table III for frequency parameters). Values in parentheses in the 3rd and 4th columns give the (60-day)/(30-day) ratios and (120-day)/(60-day) ratios of excess combined mean $\mathcal{F}$-statistic, respectively.

A common figure of merit for quantifying search sensitivity is known as the *sensitivity depth* $\mathcal{D}$ [63]:

$$\mathcal{D}(f) \equiv \frac{\sqrt{\bar{S}_h(f)}}{h_0^{95\%\ \mathrm{CL}}}, \tag{12}$$

where $\sqrt{\bar{S}_h(f)}$ is an estimate of the effective strain amplitude spectral noise density. For non-stationary detector noise, we use an inverse-noise weighted estimate for each frequency bin j from the two interferometers:

$$\bar{S}_h(f_j) = \frac{\sum_i w_{ij} S_h(f_i)}{\sum_i w_{ij}}, \tag{13}$$

where i ranges over Fourier transforms of 30-minute segments of the H1 and L1 data, and w_{ij} is a weight equal to the average inverse power spectral density for 50 neighboring frequency bins $j' \neq j$ in the same Fourier transform i:

$$w_{ij} \equiv \frac{1}{50} \sum_{j'} \frac{1}{S_h(f_{j'})} \tag{14}$$

for $|j'-j| \leq 25$ and $j' \neq j$. This weighting de-emphasizes noisy segments of data, similarly to the weighting used to define the $\mathcal{F}$-statistic. While the O3a Weave-based search [1] found an average sensitivity depth of about 74 $\mathrm{Hz}^{-\frac{1}{2}}$ over the 20-200 Hz band, we find here a depth of about 110 $\mathrm{Hz}^{-\frac{1}{2}}$ over the same range. A traditional rule of thumb in semi-coherent CW searches [23] predicts a scaling of sensitivity proportional to the fourth root of the

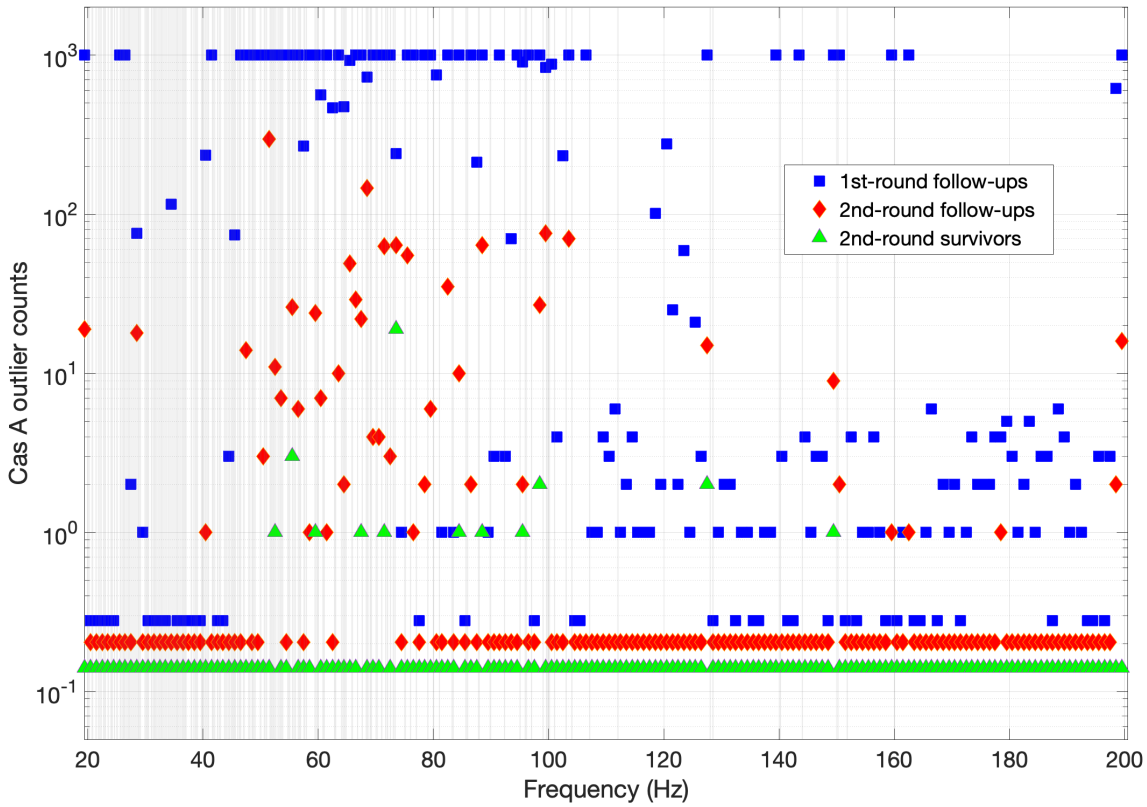

FIG. 2. Counts *vs.* frequency in 1-Hz bins for the initial Cas A search outliers (blue squares), 1st-stage follow-up survivors (red diamonds) and 2nd-stage follow-up survivors (green triangles). The vertical gray bands denote consolidated 0.1-Hz sub-bands displaying saturation in the initial search. One sees high outlier counts and saturations primarily at low frequencies contaminated by instrumental disturbances. Counts equal to zero for different stages are depicted on the vertical logarithmic scale by distinct fractions less than one (color online).

product of observation time and coherence time per segment. That overly simple rule would predict an improvement of approximately $[(11\text{ months})/(6\text{ months})]^{1/4} \times [(30\text{ days})/(5\text{ days})]^{1/4} = 1.82$. The actual improvement in depth of $\sim$1.5 is lower than that, primarily because the rule of thumb implicitly assumes a large enough number of segments that the detection statistic (in this case, a mean $\mathcal{F}$-statistic) has a normal distribution out to its 5% tails, which is not well satisfied even by the 36 segments used in the O3a analysis, much less by the 11 segments used in the initial stage of this search. A further degradation in expected depth came from the increase in statistical trials factor (semi-coherent template count) by a value of about 80 at 20 Hz to about 190 at 200 Hz from the O3a to the full-O3 search.

V. CONCLUSIONS

We have performed the deepest search to date for continuous gravitational waves from a compact star in the center of the Cassiopeia A supernova remnant. Our search yieded no detections.

The achieved 95% confidence level upper limits are well below the age-based strain amplitude limits for these stars over virtually the search band of 20–200 Hz. These upper limits are shown in Figure 4 and reach to a median strain magnitude as low as $\sim 4\times10^{-26}$ for frequencies near 200 Hz at 95% confidence level. Conservative uncertainty bands of typically $\pm 8\%$ are indicated, to account for uncertainties in strain calibration added in quadrature to statistical errors in determining individual upper limits.

We have achieved the best sensitivity to date for this source in this low-frequency band, reaching about 1.5 times below the most sensitive previous results from the LVK search in the O3a data [1], in keeping with expectation for the longer observation period and longer coherence time used in this analysis.

These sensitivities are translated from strain to equatorial ellipticity ϵ using Equation 5, assuming a source distance of 3.3 kpc for Cas A, as shown in Fig. 5. Under an r-modes emission assumption, the strain sensitivities

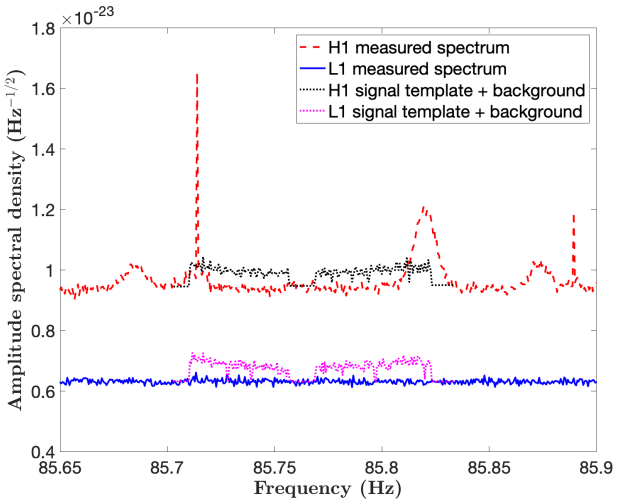

FIG. 3. Example of "strain histogram" graph for Cas A used in assessing outliers for which instrumental contamination is apparent. The curves show the O3-run-averaged H1 (red dashed) and L1 (blue solid) amplitude spectral densities in a narrow band containing artifacts near 85.7 and 85.8 Hz. The dotted curves show histograms of expected strain excess from H1 (black) and L1 (magenta) signal templates added to smooth backgrounds interpolated from neighboring frequency bands. To make the putative signal structure more apparent, the signal amplitude has been artifically magnified to $h_0 = 2 \times 10^{-24}$ (assuming circular polarization). The gap seen in the center of the signal template is due to the 1-month commissioning break in October 2019. (color online).

can similarly be translated to r-mode amplitude α, also shown in Fig. 5.

As the LIGO, Virgo and KAGRA gravitational wave detectors improve their strain sensitivities in the coming decade [64], searches will probe still smaller neutron star deformations, offering improved prospects of discovery.

VI. ACKNOWLEDGMENTS

We gratefully acknowledge useful discussions and long collaboration with current and former colleagues in the LIGO-Virgo-KAGRA continuous waves working group. For these results, in particular, we thank Evan Goetz, Ansel Neunzert, and Grant Weldon for spectral line investigations of the O3 data. We also thank Karl Wette for spearheading the development of the Weave pipeline and for helpful comments on this manuscript. This work was supported in part by National Science Foundation Award PHY-2110181.

This material is based upon work supported by NSF's LIGO Laboratory which is a major facility fully funded by the National Science Foundation. The authors are grateful for computational resources provided by LIGO Laboratory supported by the National Science Foundation Grants PHY-0757058 and PHY-0823459. This research was done using services provided by the OSG Consortium [8–11] which is supported by the National Science Foundation awards #2030508 and #1836650.

This research has made use of data or software obtained from the Gravitational Wave Open Science Center (gwosc.org) [65], a service of the LIGO Scientific Collaboration, the Virgo Collaboration, and KAGRA. This material is based upon work supported by NSF's LIGO Laboratory which is a major facility fully funded by the National Science Foundation, as well as the Science and Technology Facilities Council (STFC) of the United Kingdom, the Max-Planck-Society (MPS), and the State of Niedersachsen/Germany for support of the construction of Advanced LIGO and construction and operation of the GEO600 detector. Additional support for Advanced LIGO was provided by the Australian Research Council. Virgo is funded, through the European Gravitational Observatory (EGO), by the French Centre National de Recherche Scientifique (CNRS), the Italian Istituto Nazionale di Fisica Nucleare (INFN) and the Dutch Nikhef, with contributions by institutions from Belgium, Germany, Greece, Hungary, Ireland, Japan, Monaco, Poland, Portugal, Spain. KAGRA is supported by Ministry of Education, Culture, Sports, Science and Technology (MEXT), Japan Society for the Promotion of Science (JSPS) in Japan; National Research Foundation (NRF) and Ministry of Science and ICT (MSIT) in Korea; Academia Sinica (AS) and National Science and Technology Council (NSTC) in Taiwan.

This document has been assigned LIGO Laboratory document number `LIGO-P2400236-v2`.

APPENDIX: SATURATED SUB-BANDS

As noted above, some frequency bands were so badly contaminated by instrumental lines that one or more candidate top-lists from ($\dot{f}$, $\ddot{f}$) sub-ranges are saturated ($\geq$1000 candidates) in the initial search. All 0.1-Hz bands with saturation in at least one sub-range are listed in a consolidated format in Table V and were visually examined to verify substantial instrumental contamination. In most cases a run-averaged spectrum revealed obvious spectral artifacts, typically sharp lines in the H1 data. In a small fraction of cases there was no obvious line, but the ratio of excess mean H1 $\mathcal{F}$-statistic to excess mean L1 $\mathcal{F}$-statistic for the loudest outlier in the band was grossly inconsistent with an astrophysical source. The upper limits shown in Fig. 4 explicitly exclude these 0.1-Hz sub-bands, which sum to 26.2 Hz over the full search range of 20–200 Hz. Outliers in other, non-saturated sub-ranges of the saturated 0.1-Hz sub-bands were also followed up, but no survivors found.

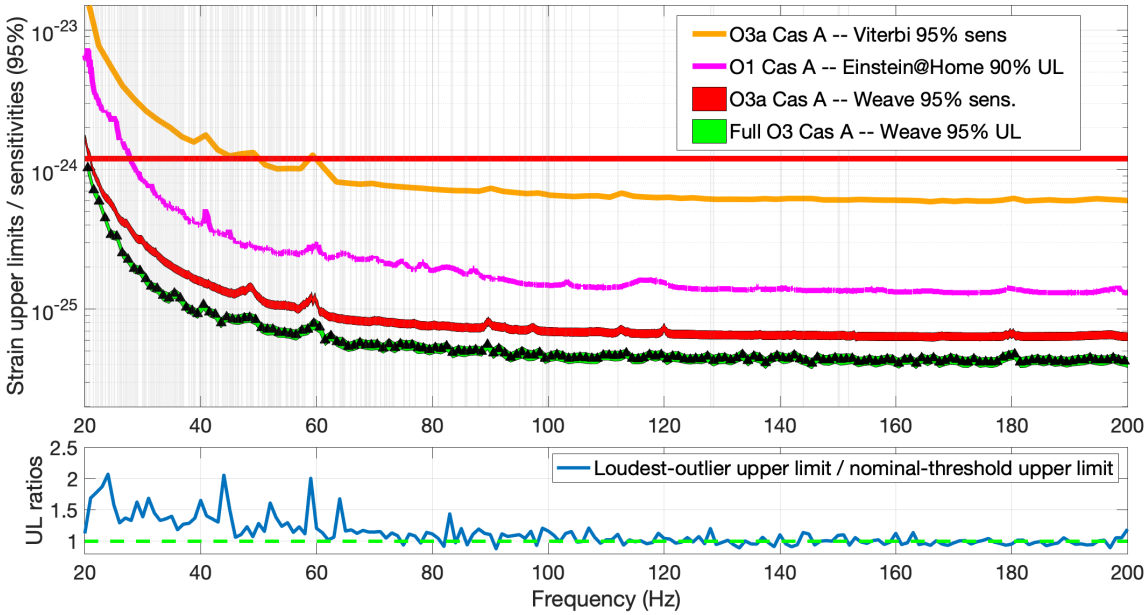

FIG. 4. *Upper panel:* Upper limits (95% confidence level) on Cas A gravitational strain amplitude in 1-Hz bands for this search and upper limits or sensitivities for several previous Cas A searches. Black triangles show upper limits based on the nominal, frequency-dependent $\mathcal{F}$-statistic threshold since all outliers above threshold were eliminated. The light green band indicates the uncertainty due to calibration added in quadrature with the statistical uncertainty due to the upper limit determination from signal injections. Vertical gray bars indicate 0.1-Hz bands in which at least one $(\dot{f},\ddot{f})$ sub-range was saturated. Although outliers were followed up in non-saturated sub-ranges of those 0.1-Hz sub-bands and eliminated, upper limits shown exclude those sub-bands, which are listed in the appendix. Also shown are the estimated 95% sensitivities for the O3a Cas A search [1] along with their uncertainties (magenta band). Conservative uncertainty bands of ±8% are indicated, to account for statistical and systematic uncertainties in estimating sensitivity depths, including calibration uncertainties. Additional results from prior searches for Cas A are also shown: O1 Einstein@Home 90% C.L. upper limits for Cas A (magenta curve) [16]; and O3a Cas A 95% C.L. upper limits using a model-robust Viterbi method (orange curve) [19]. The solid red horizontal line indicates the age-based indirect upper limit on Cas A strain amplitude.
Lower panel: Since the follow-up procedure does not achieve 100% efficiency for true signals slightly above threshold, for completeness and to be conservative, we also show the ratios of the upper limits obtained instead from the loudest (eliminated) outliers divided by the upper limits obtained from the nominal threshold. At low frequencies, where instrumental artifacts abound, the ratios range as high as 2.1, but at higher frequencies one sees small upward and downward fluctuations away from unity, where downward fluctuations occur for bands with no outliers above threshold or with a loudest outlier barely above threshold and for which statistical errors between independently determined upper limits dominate.

[1] R. Abbott *et al.*(LIGO-Virgo Collaboration), Search of the Early O3 LIGO Data for Continuous Gravitational Waves from the Cassiopeia A and Vela Jr. Supernova Remnants, Phys. Rev. D **105**, 082005 (2022).

[2] M. Ryle and F.G. Smith, A New Intense Source of Radio-Frequency Radiation in the Constellation of Cassiopeia, Nat. **162**, 462 (1948).

[3] A.F. Iyudin *et al.*, Emission from ^{44}Ti associated with a previously unknown Galactic supernova, Nat. **396**, 142 (1998).

[4] K. Wette *et al.*, Implementing a semicoherent search for continuous gravitational waves using optimally-constructed template banks, Phys. Rev. D **97**, 123016 (2018).

[5] J. Aasi *et al.* (LIGO Scientific Collaboration), Advanced LIGO, Class. Quantum Grav. **32** 074001 (2015).

[6] F. Acernese *et al.*(Virgo Collaboration), Advanced Virgo: a 2nd generation interferometric gravitational wave detector, Class. Quantum Grav. **32** 024001 (2015).

[7] T.Akutsu *et al.*, Overview of KAGRA: Detector design and construction history, Prog. Theor. Expt. Phys. **2021**, 05A101 (2021).

[8] R. Pordes, D. Petravick, B. Kramer, D. Olson, M. Livny, A. Roy, P. Avery, K. Blackburn, T. Wenaus, F. Würthwein, I. Foster, R. Gardner, M. Wilde, A. Blatecky, J. McGee, and R. Quick, The open science grid, J. Phys. Conf. Ser. **78**, 012057 (2007), https://doi.org/10.1088/1742-6596/78/1/012057.

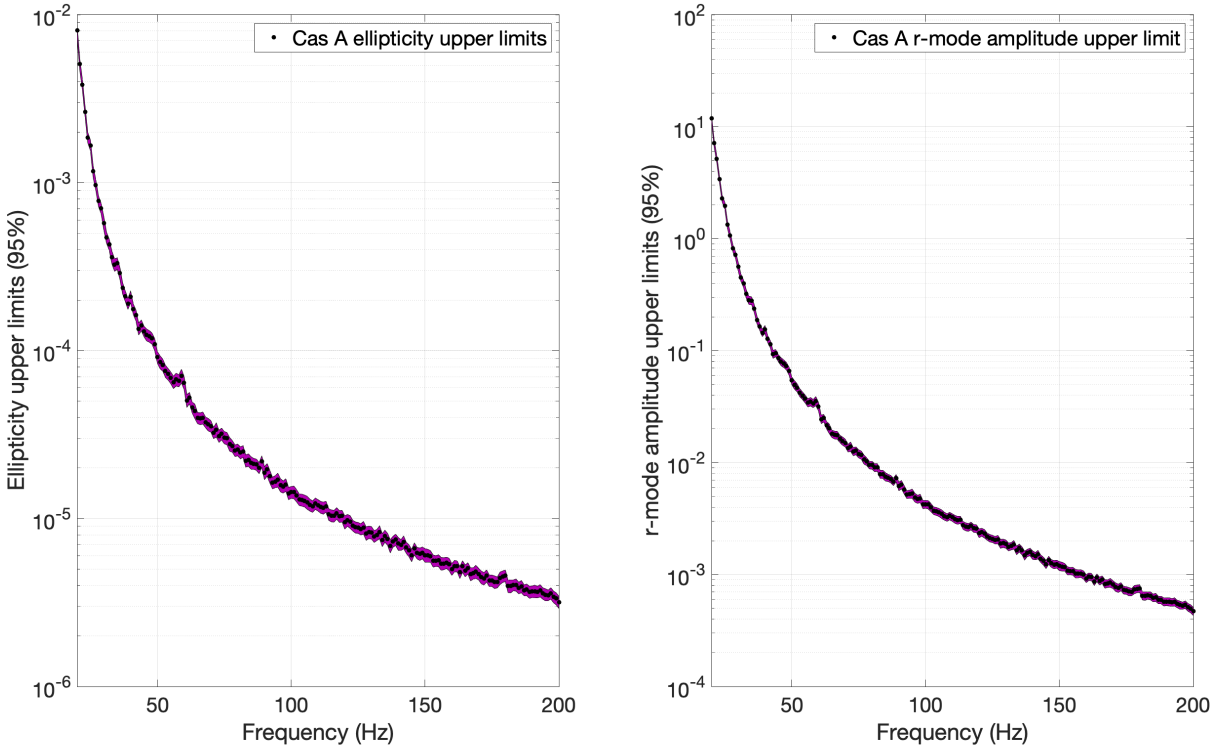

FIG. 5. *Left panel:* Upper limits on equatorial ellipticity (95% C.L.) in each 1-Hz band for the Cas A search derived from the strain amplitude upper limits shown in Fig. 4 assuming a source distance of 3.3 kpc for Cas A. *Right panel:* Upper limits on r-modes amplitude α (95% C.L.) in each 1-Hz band for the Cas A search, derived from the strain upper limits.

[9] I. Sfiligoi, D.C. Bradley, B. Holzman, P. Mhashilkar, S. Padhi and F. Wurthwein, (2009). The pilot way to grid resources using glideinWMS. 2009 WRI World Congress on Computer Science and Information Engineering, 2, 428–432. https://doi.org/10.1109/CSIE.2009.950.

[10] OSG. (2006). OSPool. OSG. https://doi.org/10.21231/906P-4D78.

[11] OSG. (2015). Open Science Data Federation. OSG. https://doi.org/10.21231/0KVZ-VE57.

[12] D.R. Lorimer and M. Kramer, Handbook of Pulsar Astronomy, Cambridge University Press, Cambridge, UK (2005).

[13] J. Abadie *et al.*(LIGO-Virgo Collaboration), First search for gravitational waves from the youngest known neutron star, Astroph. J. **722**, 1504 (2010).

[14] J. Aasi *et al.*(LIGO-Virgo Collaboration), Astroph. J **813**, 39 (2015).

[15] B.P. Abbott *et al.*(LIGO-Virgo Collaboration), Searches for Continuous Gravitational Waves from 15 Supernova Remnants and Fomalhaut b with Advanced LIGO, Astroph. J. **875**, 122 (2019).

[16] J. Ming *et al.*, Results from an Einstein@Home search for continuous gravitational waves from Cassiopeia A, Vela Jr. and G347.3, Phys. Rev. D", **100**, 024063 (2019).

[17] M.A. Papa *et al.*, Search for Continuous Gravitational Waves from the Central Compact Objects in Supernova Remnants Cassiopeia A, Vela Jr., and G347.3–0.5, Astrophys. J. **897**, 22 (2020).

[18] M. Millhouse, L. Strang and A. Melatos, Search for gravitational waves from twelve young supernova remnants with a hidden Markov model in Advanced LIGO's second observing run, Phys. Rev. D **102**, 083025 (2020).

[19] R. Abbott *et al.*(LIGO-Virgo-KAGRA Collaboration), Searches for continuous gravitational waves from young supernova remnants in the early third observing run of Advanced LIGO and Virgo, Astrophys. J. **921**, 80 (2021).

[20] M. Sieniawska and M. Bejger, Continuous gravitational waves from neutron stars: current status and prospects, Universe **5**, 217 (2019).

[21] R. Tenorio, D. Keitel and A. Sintes, Search Methods for Continuous Gravitational-Wave Signals from Unknown Sources in the Advanced-Detector Era, Universe **7**, 474 (2021).

[22] O.J. Piccinni, Status and Perspectives of Continuous Gravitational Wave Searches, Galaxies **10**, 72 (2022).

[23] K. Riles, Searches for continuous-wave gravitational radiation, Liv. Rev. Rel. **26** 3 (2023).

[24] K. Wette, Searches for continuous gravitational waves from neutron stars: A twenty-year retrospective, Astropart. Phys. **153** 102880 (2023).

[25] D.W. Hughes, Did Flamsteed see the Cassiopeia A supernova?, Nat. **285**, 132 (1980).

[26] R.A. Fesen *et al.*, The Expansion Asymmetry and Age of the Cassiopeia A Supernova Remnant, Astroph. J, 645, 283

$f_{\rm low}$ (Hz)	Δf (Hz)	$f_{\rm low}$ (Hz)	Δf (Hz)	$f_{\rm low}$ (Hz)	Δf (Hz)	$f_{\rm low}$ (Hz)	Δf (Hz)	$f_{\rm low}$ (Hz)	Δf (Hz)	$f_{\rm low}$ (Hz)	Δf (Hz)	$f_{\rm low}$ (Hz)	Δf (Hz)	$f_{\rm low}$ (Hz)	Δf (Hz)	$f_{\rm low}$ (Hz)	Δf (Hz)
20.0	0.3	26.6	0.1	36.3	0.2	42.8	0.3	50.6	0.1	57.5	0.2	68.6	0.1	80.0	0.1	103.0	0.1
20.7	0.2	26.9	0.2	36.6	0.2	43.7	0.4	50.9	0.2	57.9	0.1	69.0	0.1	81.0	0.1	104.0	0.1
21.4	0.1	27.2	1.6	36.9	0.2	44.3	0.4	51.6	0.2	59.4	0.3	69.2	0.1	83.2	0.3	107.1	0.1
21.8	0.6	28.9	0.3	37.9	0.2	44.9	0.2	51.9	0.3	59.9	0.1	70.0	0.3	85.6	0.4	112.0	0.1
22.7	0.2	29.9	0.2	38.4	0.1	45.2	0.2	52.3	0.4	60.8	0.1	71.0	0.1	87.8	0.2	128.0	0.1
23.0	0.1	30.2	0.2	38.7	0.1	45.5	0.2	53.0	0.1	61.0	0.1	71.7	0.1	89.8	0.2	128.5	0.1
23.5	0.1	30.5	0.1	38.9	0.2	46.0	0.1	53.3	0.2	62.8	0.1	72.0	0.1	92.3	0.1	140.2	0.1
24.0	0.1	31.0	0.1	39.7	0.1	46.3	0.1	53.6	0.3	63.0	0.1	72.5	0.1	95.0	0.1	144.0	0.1
24.2	0.1	31.3	0.3	39.9	0.2	46.5	0.1	54.7	0.1	64.0	0.5	73.0	0.1	95.9	0.3	150.0	0.3
24.6	0.1	31.7	0.4	40.3	0.3	47.0	0.2	54.9	0.2	64.6	0.3	73.3	0.1	97.0	0.1	151.8	0.1
25.0	0.2	32.3	0.5	40.8	0.2	47.9	0.3	55.5	0.2	65.8	0.2	75.0	0.2	99.0	0.1	160.0	0.1
25.6	0.1	32.9	0.8	41.6	0.1	48.5	0.1	55.9	0.2	66.8	0.1	76.0	0.1	99.6	0.1		
25.9	0.3	33.9	1.6	41.8	0.3	48.7	0.4	56.5	0.3	67.6	0.1	77.0	0.1	99.8	0.4		
26.3	0.1	35.6	0.5	42.5	0.1	49.9	0.2	56.9	0.1	68.3	0.2	79.0	0.1	101.0	0.1		

TABLE V. Frequency bands with saturation in the first stage of the Cas A search ($\geq$1000 outliers above threshold in a 0.1-Hz band for at least one sub-range ($\dot{f}$,$\ddot{f}$) of frequency derivatives. Each pair of numbers gives the lower limit of frequency and the width of the band affected. Consecutive 0.1-Hz bands are concatenated for compactness. These bands are excluded from the Cas A upper limits shown in Fig. 4

[27] M. Ruderman, Neutron starquakes and pulsar periods, Nat. **223**, 597 (1969).

[28] G. Baym *et al.*, Spin up in neutron stars: The future of the vela pulsar, Nat. **224**, 872 (1969).

[29] V,R. Pandharipande, D. Pines and R.A. Smith, Neutron star structure: theory, observation, and speculation, Astroph. J. **208**, 550 (1976).

[30] M. Zimmermann, Revised estimate of gravitational radiation from Crab and Vela pulsars, Nat. **271**, 524, (1978).

[31] C. Cutler, Gravitational waves from neutron stars with large toroidal B fields, Phys. Ref. D **66**, 084025 (2002).

[32] B. Haskell *et al.*, Detecting gravitational waves from mountains on neutron stars in the Advanced Detector Era, Mon. Not. Roy. Astron. Soc. **450**, 2393 (2015).

[33] F.J. Fattoyev, C.J. Horowitz and H. Lu, Crust breaking and the limiting rotational frequency of neutron stars, arXiv:1804.04952, April 2018.

[34] N. Singh *et al.*, Asymmetric accretion and thermal 'mountains' in magnetized neutron star crusts, Mon. Not. Roy. Astron. Soc. **493**, 3866 (2020).

[35] N. Andersson, A New class of unstable modes of rotating relativistic stars, Astroph. J. **502**, 708 (1998).

[36] L. Bildsten, Gravitational radiation and rotation of accreting neutron stars, Astroph. J. Lett. **501**, L89 (1998).

[37] J.L. Friedman and S.M. Morsink, Axial instability of rotating relativistic stars, Astroph. J. **502**, 714 (1998).

[38] B.J. Owen *et al.*, Gravitational waves from hot young rapidly rotating neutron stars, Phys. Rev. D **58**, 084020 (1998).

[39] Y. Kojima, Quasitoroidal oscillations in rotating relativistic stars, Mon. Not. Roy. Astron. Soc. **293**, 49 (1998).

[40] P. Lasky, Gravitational waves from neutron stars: A review, Pub. Astron. Soc. Aust. **32**, e034 (2015).

[41] K. Glampedakis and L. Gualtieri, Gravitational waves from single neutron stars: an advanced detector era survey, Astroph. Space Sci. Lib. **457** 673-736 (2018).

[42] K. Wette *et al.*, Searching for gravitational waves from Cassiopeia A with LIGO, Class. Quant. Grav. **25**, 235011 (2008).

[43] H. Tananbaum, Cassiopeia A, I.A.U. Circ. **7246**, 1 (1999).

[44] W. Ho *et al.*, X-ray bounds on cooling, composition, and magnetic field of the Cassiopeia A neutron star and young central compact objects, Mon. Not. Roy. Astron. Soc. **506**, 5015 (2021).

[45] J.P. Halpern and E.V. Gotthelf, Spin-Down Measurement of PSR J1852+0040 in Kesteven 79: Central Compact Objects as Anti-Magnetars, Astroph. J. **709**, 436 (2010).

[46] J.E. Reed *et al.*, The three-dimensional structure of the Cassiopeia A Supernova Remnant. I. The spherical shell, Astroph. J. **440**, 706 (1995).

[47] A. Alarie, A. Bilodeau and L. Drissen, A hyperspectral view of Cassiopeia A, Mon. Not. Roy. Astron. Soc. **441**, 2996 (2014).

[48] P. Jaranowski, A. Krolak and B.F. Schutz, Data analysis of gravitational-wave signals from spinning neutron stars. 1. The Signal and its detection, Phys. Rev. D **58**, 063001 (1998).

[49] L. Sun *et al.*, Characterization of systematic error in Advanced LIGO calibration, Class. Quant. Grav. **37**, 225008 (2020).

[50] P. Covas *et al.*, Identification and mitigation of narrow spectral artifacts that degrade searches for persistent gravitational waves in the first two observing runs of Advanced LIGO, Phys. Rev. D **97** 082002 (2018).

[51] E. Goetz *et al.*, O3 lines and combs in found in self-gated C01 data `https://dcc.ligo.org/LIGO-T2100200/public`.

[52] R. Abbott *et al.*(LIGO-Virgo Collaboration), All-sky Search for Continuous Gravitational Waves from Isolated Neutron Stars in the Early O3 LIGO Data, Phys. Rev. D **104**, 082004 (2021).

[53] J. Zweizig and K. Riles, Information on self-gating of $h(t)$ used in O3a continuous-wave searches, LIGO Technical Report T2000384, September 2020, `https://dcc.ligo.org/LIGO-T2000384/public`.

[54] D. Davis *et al.*, LIGO Detector Characterization in the Second and Third Observing Runs, Class. Quant. Grav. **38**, 135014 (2021).

[55] B.P. Abbott *et al.* (LIGO Scientific Collaboration), All-sky search for periodic gravitational waves in LIGO S4 data, Phys. Rev. D **77**, 022001 (2008).

[56] B.J. Owen, How to adapt broad-band gravitational-wave searches for r-modes, Phys. Rev. D **82**, 104002 (2010)

[57] http://simbad.u-strasbg.fr/simbad Object CXOU J232327.8+584842 (J2000).

[58] K. Wette and R. Prix, Flat parameter-space metric for all-sky searches for gravitational-wave pulsars, Phys. Rev. D **88**, 123005 (2013).

[59] K. Wette, Parameter-space metric for all-sky semi-coherent searches for gravitational-wave pulsars, Phys. Rev. D **92**, 082003 (2015).

[60] K. Wette, Lattice template placement for coherent all-sky searches for gravitational-wave pulsars, Phys. Rev. D **90**, 122010 (2014).

[61] M. Capó, A. Pérez, and J.A. Lozano, An efficient K-means clustering algorithm for massive data, Data Mining and Know. Disc. **34**, 776 (2020).

[62] K-means clustering algorithm ("lloyd") implementation drawn from the scikit python library: https://scikit-learn.org/stable/modules/generated/sklearn.cluster.KMeans.html.

[63] B. Benhke, M.A. Papa and R. Prix, Postprocessing methods used in the search for continuous gravitational-wave signals from the Galactic Center, Phys. Rev. D **91**, 064007 (2015).

[64] B.P. Abbott *et al.* (LIGO-Virgo-KAGRA Collaboration), Prospects for Observing and Localizing Gravitational-Wave Transients with Advanced LIGO, Advanced Virgo and KAGRA Liv. Rev. Rel. **23**, 3 (2020).

[65] Gravitational Wave Open Science Center, `https://www.gw-openscience.org`; see also: R. Abbott *et al.*(LIGO Scientific Collaboration, Virgo Collaboration and KAGRA Collaboration), Open data from the third observing run of LIGO, Virgo, KAGRA and GEO", Astro. J. S. **267**, 29 (2023).